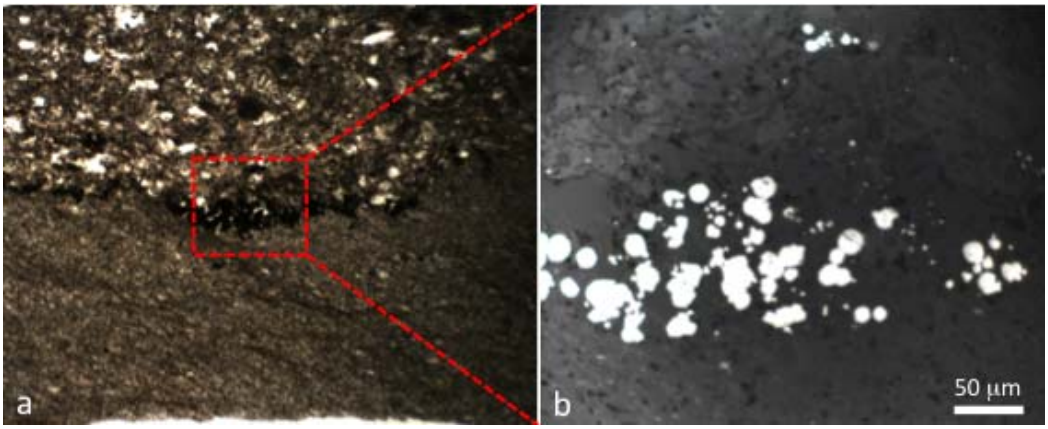


**Figure DR1.** Occurrence of putative framboidal pyrite from the late Ediacaran of the Catalina Dome, Bonavista Peninsula, Newfoundland (sample WM1, c. 560 Ma Fermeuse Formation). a) Thin section in plane-polarised light showing how framboidal pyrite typically occurs on bedding plane surfaces between a lower mudstone and an upper coarser siltstone or reworked volcanic ash. Impressions of Ediacaran organisms such as *Charniodiscus* sp. and *Bradgatia* sp. are found on this same bedding surface. Note also the wispy carbonaceous laminae that probably represent the remnants of biofilms. b) Higher magnification reflected light image, revealing that the pyrite occurs as both single sub-spherical grains and clusters of cemented and overgrown grains.

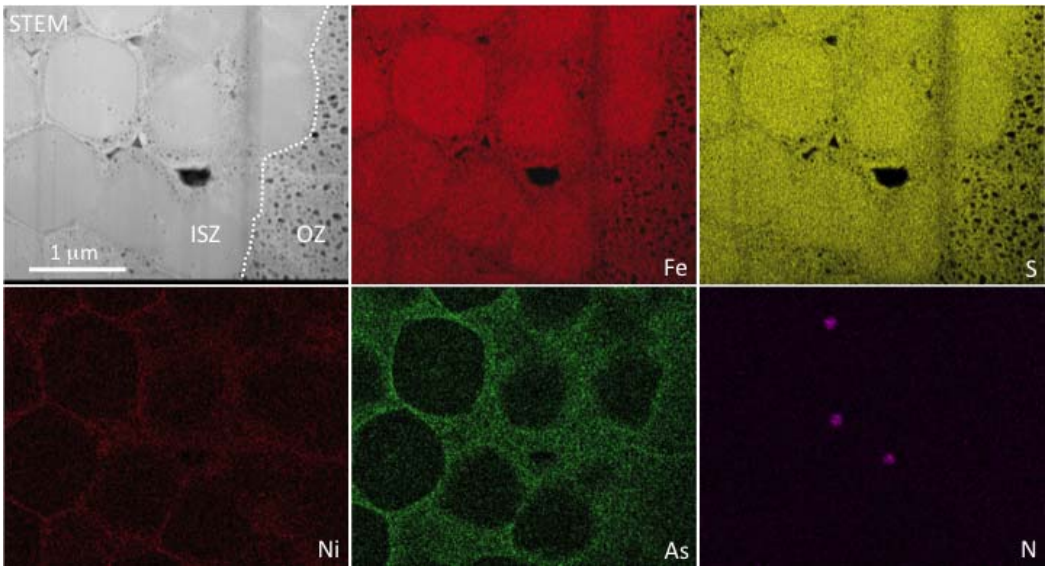


**Figure DR2.** Dark-field scanning transmission electron microscope (STEM) image, plus ChemiSTEM maps of part of a pyrite framboid (brighter colours indicate higher concentrations of each element). Arsenic and nickel are enriched in the nano-porous rims of the pyrite microcrystals in the ISZ, and also to a lesser extent in the OZ. Nitrogen is seen at

some triple junctions in the ISZ, reinforcing our NanoSIMS data. However, the overall pattern of N enrichment seen in NanoSIMS maps is not visible here. This is due to the extreme thinness of the TEM sample and the poorer detection limits for N in the TEM.

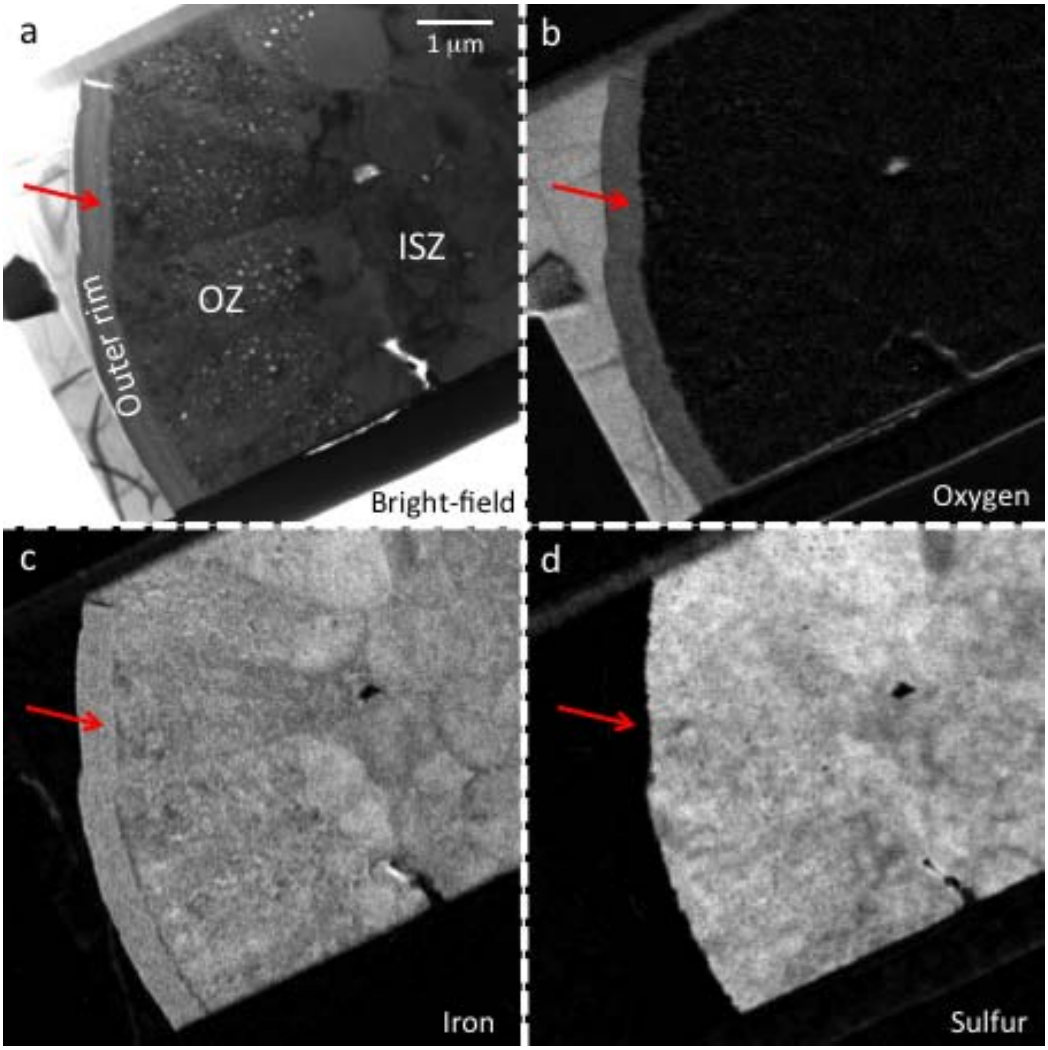


**Figure DR3.** Bright-field TEM image and energy-filtered (EFTEM) elemental maps from the outer part of a pyrite grain. While the ISZ and OZ are clearly composed of pyrite, the outer rim contains no sulfur and has been oxidised to iron oxide (arrow). The mineral to the left of the iron oxide rim is silica, hence the high oxygen signal.

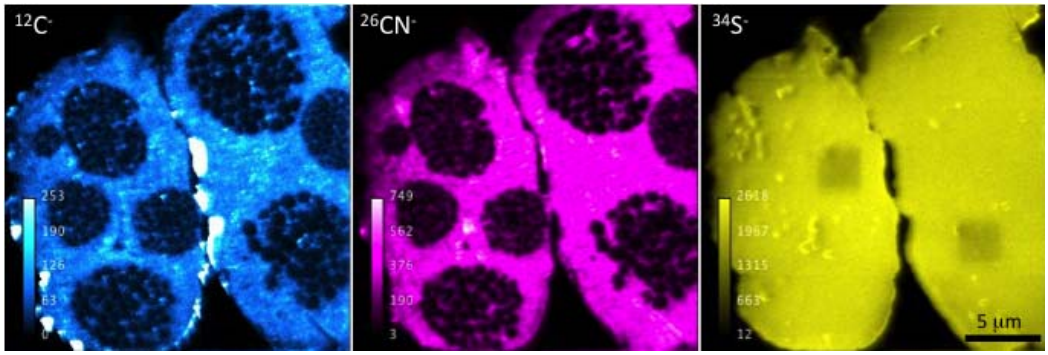


**Figure DR4.** NanoSIMS ion maps of carbon ($^{12}C^-$), nitrogen ($^{26}CN^-$) and sulfur ($^{34}S^-$) showing organic-rich pyrite overgrowth and cementation of numerous individual framboids. Note that this nano-structure is only visible in the C and CN images.

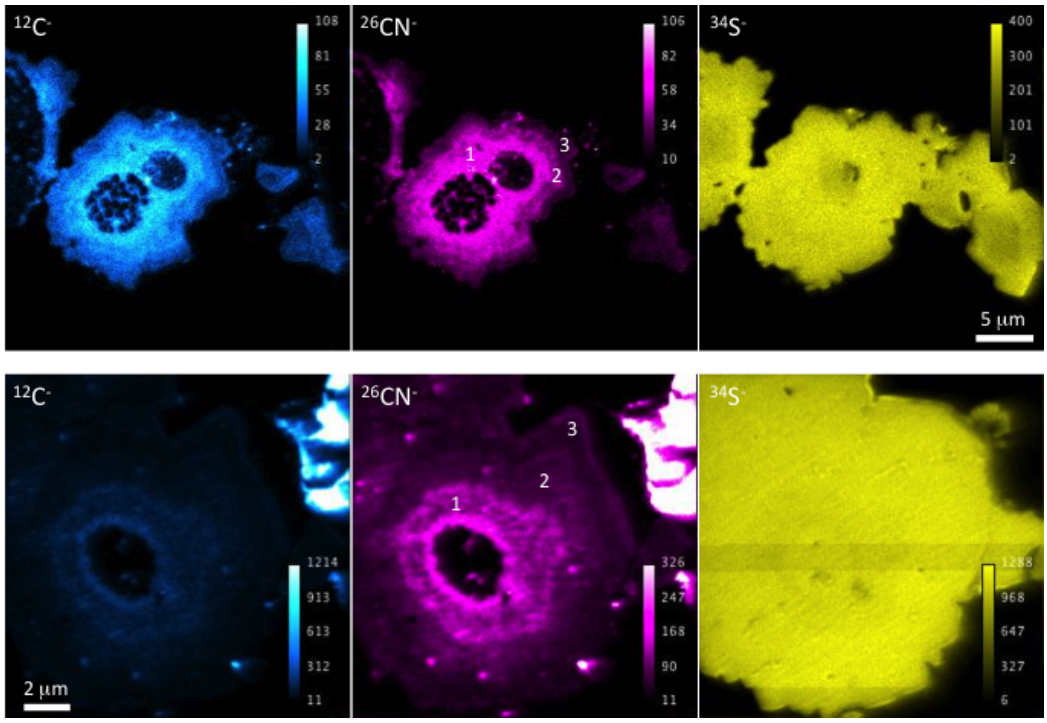


**Figure DR5.** Examples of concentric zoning of organic material in pyrite framboid overgrowths. Pyrite closest to the original framboids shows the highest concentration of organic material (1). Two further zones (2 and 3) record decreasing concentrations of organic material as the pyrite overgrowth increases in size. Note that sulfur signal is rather uniform across all zones.

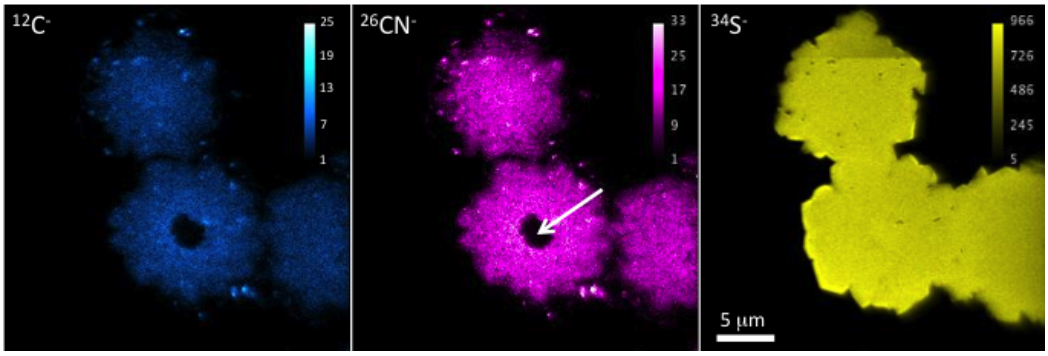


**Figure DR6.** NanoSIMS ion maps of carbon ($^{12}C^-$), nitrogen ($^{26}CN^-$) and sulfur ($^{34}S^-$) showing more poorly preserved pyrite framboids. The internal zone of micro-grains in an organic matrix is not preserved, being replaced by either a spheroidal pure pyrite core (arrow) or in other cases homogenous organic-rich pyrite.

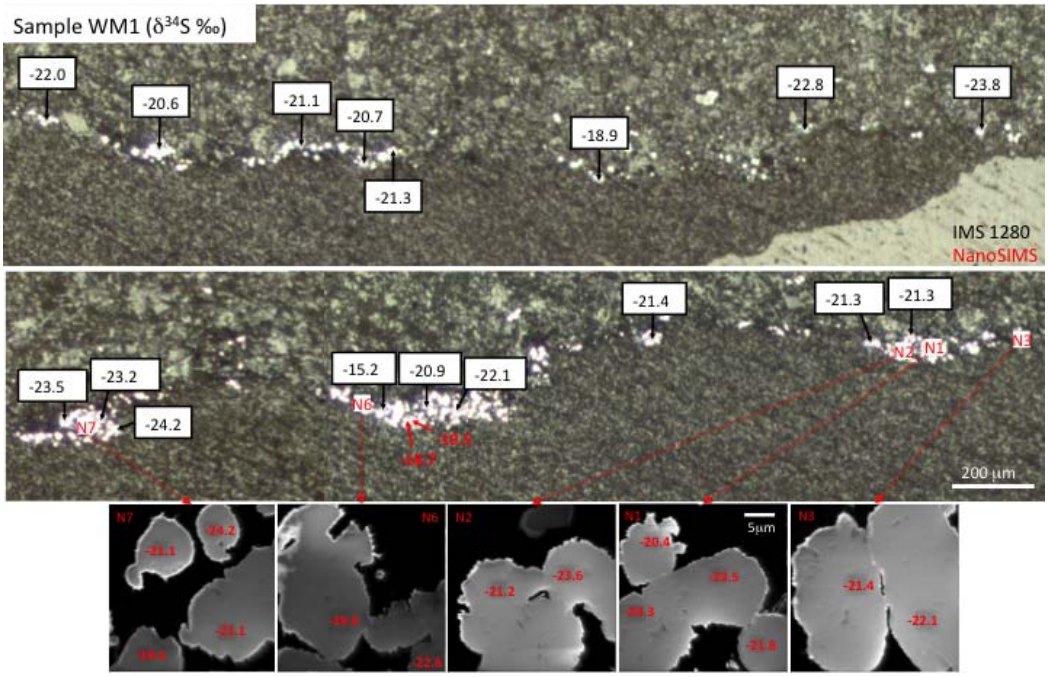


**Figure DR7.** Pictorial overview of sulfur isotope values ($\delta^{34}S$ ‰) obtained using NanoSIMS from framboidal pyrite in the c. 560 Ma Fermeuse Formation. These rather homogenous and light $\delta^{34}S$ values suggest the source of sulfur for the framboidal pyrite was microbial sulfate reduction under conditions of electron donor limitation (cf. Sim et al., 2011).

**Table DR1.** Sulfur isotope data ($\delta^{34}S_{V\text{-}CDT}$ ‰) from framboidal pyrite within the c. 560 Ma Fermeuse formation of Newfoundland (sample WM1).

| Analysis ID | $^{34}S$ counts | $\delta^{34}S_{V\text{-}CDT}$ | ±2σ (‰) |
|---|---|---|---|
| | **SESSION 1 (NANOSIMS)** | | |
| ***Standards*** | **(x10$^6$)** | | |
| SON-3_1 | 5.42 | 1.8 | 1.1 |
| SON-3_2 | 5.24 | 1.4 | 0.9 |
| SON-3_3 | 5.24 | 2.4 | 0.9 |
| SON-3_4 | 5.23 | 0.6 | 0.9 |
| SON-3_5 | 5.18 | 2.3 | 1.0 |
| SON-3_6 | 5.20 | 3.0 | 1.0 |
| SON-3_7 | 5.19 | -0.4 | 1.0 |
| SON-3_8 | 5.18 | 1.8 | 1.1 |
| SON-3_9 | 5.23 | 1.2 | 1.4 |
| SON-3_10 | 5.12 | 1.1 | 1.5 |
| SON-3_11 | 5.09 | 2.6 | 1.5 |
| | | Mean = 1.6 | |
| | | S.D. = 1.0 | |
| ***Sample WM1*** | | | |
| WM_1a | 4.75 | -21.8 | 0.9 |
| WM_1b | 5.31 | -23.5 | 0.8 |
| WM_1c | 5.13 | -20.4 | 0.8 |
| WM_2a | 4.95 | -23.6 | 0.9 |
| WM_2b | 4.95 | -21.2 | 0.9 |
| WM_3a | 5.00 | -22.1 | 0.9 |
| WM_3b | 4.82 | -21.4 | 0.9 |
| WM_5a | 4.21 | -18.7 | 1.0 |
| WM_5b | 4.71 | -19.5 | 1.0 |
| WM_6a | 4.96 | -19.4 | 1.1 |
| WM_6b | 4.97 | -22.6 | 1.1 |
| WM_7a | 5.46 | -21.1 | 1.2 |
| WM_7b | 5.13 | -24.2 | 1.2 |
| WM_7c | 5.01 | -23.1 | 1.3 |
| WM_7d | 5.13 | -19.6 | 1.3 |
| WM_1d | 5.12 | -24.3 | 1.4 |
| | **SESSION 2 (IMS 1280)** | | |
| ***Standards*** | **(x10$^{10}$)** | | |
| SON-3_1 | 1.99 | 1.57 | 0.06 |
| SON-3_2 | 1.98 | 1.57 | 0.06 |
| SON-3_3 | 1.99 | 1.66 | 0.06 |
| SON-3_4 | 1.99 | 1.58 | 0.06 |
| SON-3_5 | 2.02 | 1.60 | 0.06 |
| SON-3_6 | 2.07 | 1.67 | 0.05 |
| SON-3_7 | 2.07 | 1.60 | 0.05 |
| SON-3_8 | 2.09 | 1.66 | 0.05 |
| SON-3_9 | 2.07 | 1.61 | 0.05 |
| SON-3_10 | 2.11 | 1.63 | 0.05 |
| SON-3_11 | 2.11 | 1.65 | 0.06 |
| SON-3_12 | 2.11 | 1.66 | 0.06 |
| SON-3_13 | 2.11 | 1.56 | 0.06 |
| SON-3_14 | 2.11 | 1.55 | 0.06 |
| SON-3_15 | 2.13 | 1.58 | 0.06 |

| | | | |
|---|---|---|---|
| | | Mean = 1.61 | |
| | | SD = 0.04 | |
| FREO_1 | 1.96 | -4.49 | 0.05 |
| FREO_2 | 2.05 | -4.40 | 0.05 |
| FREO_3 | 2.07 | -4.44 | 0.06 |
| | | Mean = -4.45 | |
| | | SD = 0.05 | |
| ***Sample WM1*** | | | |
| WM_1 | 1.47 | -23.48 | 0.08 |
| WM_2 | 0.81 | -23.15 | 0.08 |
| WM_3 | 0.86 | -24.23 | 0.10 |
| WM_4 | 1.12 | -15.21 | 0.07 |
| WM_5 | 0.58 | -20.90 | 0.07 |
| WM_6 | 0.92 | -22.12 | 0.06 |
| WM_7 | 0.92 | -21.42 | 0.15 |
| WM_8 | 1.35 | -21.29 | 0.08 |
| WM_9 | 1.12 | -21.33 | 0.11 |
| WM_10 | 1.06 | -21.26 | 0.10 |
| WM_11 | 0.40 | -20.71 | 0.16 |
| WM_12 | 0.65 | -21.13 | 0.12 |
| WM_13 | 1.33 | -20.60 | 0.08 |
| WM_14 | 1.15 | -22.00 | 0.06 |
| WM_15 | 0.65 | -18.85 | 0.12 |
| WM_16 | 0.40 | -22.76 | 0.09 |
| WM_17 | 0.50 | -23.75 | 0.17 |

## Methods

*Focussed ion beam (FIB) preparation of TEM samples*

A dual-beam FIB system (FEI Helios NanoLab) at the Electron Microscopy Unit, University of New South Wales was used to prepare pyrite framboid TEM samples from standard uncovered polished geological thin sections coated with c.30 nm of gold. Electron beam imaging was used to identify framboids of interest in the polished thin sections allowing site-specific TEM samples to be prepared. The TEM sections were prepared by a series of steps involving different beam energies and currents (see Wacey et al., 2012), resulting in ultrathin wafers of c. 100 nm thickness. These TEM wafers were extracted using an ex-situ micromanipulator and deposited on continuous-carbon copper TEM grids. FIB preparation of TEM sections allows features below the surface of the thin sections to be targeted, thus eliminating the risk of surface contamination producing artefacts.

*TEM analysis of FIB-milled wafers*

TEM data were obtained using a *FEI Titan G2 80-200* TEM/STEM with *ChemiSTEM Technology* operating at 200 kV, plus a *JEOL 2100* $LaB_6$ TEM operating at 200 kV equipped with a *Gatan Orius* CCD camera and *Tridiem* energy filter. Both instruments are located in the Centre for Microscopy, Characterisation and Analysis (CMCA) at The University of Western Australia. HAADF (high angle annular dark-field) STEM images and EDS (*ChemiSTEM*) maps were obtained on the *FEI Titan*. Energy filtered (EFTEM) elemental maps were obtained on the *JEOL 2100* using the

conventional three-window technique (Brydson, 2001), with energy windows selected to provide optimum signal-to-noise.

*NanoSIMS ion mapping*

I

on mapping was performed using a CAMECA NanoSIMS 50 at CMCA, The University of Western Australia, with instrument parameters optimized as described in Wacey et al. (2011). Analysis areas varied from 12 x 12 μm up to 30 x 30 μm, at a resolution of 256 x 256 pixels (each pixel measuring between 47 nm and 117 nm, depending on the image area), with a dwell time of 20 ms per pixel, and a primary beam current of c.2.5 pA. Secondary ions mapped were $^{12}C^-$, $^{26}CN^-$, and $^{34}S^-$ (note the use of $^{34}S^-$ instead of $^{32}S^-$, because $^{32}S^-$ provided too many counts to the electron multiplier detector at the conditions required for good $^{12}C^-$ and $^{26}CN^-$ imaging), and charge compensation was achieved by using the electron flood gun.

*NanoSIMS sulfur isotope analysis*

Sulfur isotope ratios ($^{34}S/^{32}S$) from individual pyrite grains were determined using a CAMECA NanoSIMS 50 at CMCA, The University of Western Australia. The analyses were performed using a Faraday Cup (FC) detector for the $^{32}S$ signal and an electron multiplier (EM) for the $^{34}S$ signal, with a primary beam current of c.2.5 pA, and a raster area of 3 x 3 μm. Instrument setup, data acquisition, drift correction, instrumental mass fractionation correction and error propagation were carried out according to the protocol described in McLoughlin et al. (2012). All samples were confirmed as pyrite using laser Raman spectroscopy, so no corrections for matrix effects between the samples and our SON-3 pyrite standard were applied. Analyses were completed over a single analytical session with an uncertainty on bracketing $\delta^{34}S$ standard analyses of 1.0 ‰ (1SD; n = 11). Propagated errors for individual analyses ($2\sigma$) are listed in the final column of Table DR1.

*IMS 1280 sulfur isotope analysis*
*Instrument setup*

Sulfur isotope ratios ($^{34}S/^{32}S$) were determined using a CAMECA IMS 1280 ion microprobe operating in multi-collection mode at CMCA, The University of Western Australia. In all cases NMR regulation was used and $^{32}S$ and $^{34}S$ were measured using Faraday cup detectors (FC). A rastered beam approach employing dynamic transfer was used. A 3.5 nA focused primary beam was used to pre-sputter the analysis area using a 30 μm × 30 μm beam for 40 seconds followed by automated secondary centering in the field aperture (FA) and entrance slit (ES); and analysis using a 20 μm × 20 μm raster employing dynamic transfer for 45 × 4 second integrations. Unknowns were bracketed with standards of known composition. Other conditions include a 133 × magnification between sample stage and field aperture (FA), 70 μm entrance slit, 4000 μm FA, 400 μm contrast aperture, a 40 eV energy window with a 5 eV offset to the high energy side, and 500 μm exit slits. Although the pyrite targets are conductors, the normal incidence electron flood gun was utilized for charge compensation in the event that the primary ion beam overlapped onto insulating matrix silica minerals. External precision of $^{34}S/^{32}S$ on the SON-3 standard for the analytical session was better than 0.05 ‰ (1 SD; n = 15). A secondary standard (FREO) was run as an unknown in some cases. These samples returned a

mean value of -4.45 ± 0.05 ‰ (1 SD, n = 3), which is in good agreement with the laser fluorination value of -4.3 ‰. Sample count rates varied between ~20 % and 75 % of the count rate of the standard, however, there was no observed correlation between secondary count rate and $\delta^{34}S$ of the samples.

*Data processing*

Instrumental mass fractionation and propagation of uncertainty follow the protocol in Farquhar et al. (2013). Uncertainty terms included internal uncertainty, external uncertainty of the instrumental mass fractionation of the primary standard, and uncertainty of the standard relative to V-CDT.

**References**


Brydson, R., 2001, *Electron Energy Loss Spectroscopy*: Springer-Verlag, New York.

Farquhar, J., Cliff, J., Zerkle, A.L., Kamyshny, A., Poulton, S.W., Claire, M., Adams, D., and Harms, B., 2013, Pathways for Neoarchean pyrite formation constrained by mass-independent sulfur isotopes: Proceedings of the National Academy of Sciences USA, v. 110, p. 17638-17643.

McLoughlin, N., Grosch, E.G., Kilburn, M.R, and Wacey, D., 2012, Sulfur isotope evidence for a Paleoarchean subseafloor biosphere, Barberton, South Africa: Geology, v. 40, p. 1031–1034.

Sim, M.S., Bosak, T., and Ono, S., 2011, Large sulfur isotope fractionation does not require disproportionation: Science, v. 333, p. 74–77.

Wacey D., Kilburn, M.R., Saunders, M., Cliff, J., and Brasier, M.D., 2011, Microfossils of sulphur-metabolizing cells in 3.4 billion-year-old rocks of Western Australia: Nature Geoscience, v. 4, p. 698–702.

Wacey, D., Menon, S., Green, L., Gerstmann, D., Kong, C., McLoughlin, N., Saunders, M., and Brasier, M.D., 2012, Taphonomy of very ancient microfossils from the ~3400 Ma Strelley Pool Formation and ~1900 Ma Gunflint Formation: new insights using focused ion beam: Precambrian Research, v. 220-221, p. 234–250.